Elimination of Harmonic Currents Using a Reference Voltage Vector Based-Model Predictive Control for a Six-Phase PMSM Motor

Yixiao Luo, *Student Member, IEEE*, and Chunhua Liu, *Senior Member, IEEE*

***Abstract*—This paper proposes a novel deadbeat current control (DBCC)-based model predictive control for an asymmetrical six-phase permanent magnet synchronous machine. First, the solution of DBCC is adopted to obtain the expected reference voltage vector (RVV). Then, two groups of virtual vectors, in the total number of 24 with different magnitudes, are defined for the sake of current harmonics suppression. Subsequently, two in-phase virtual vectors which are closest to the RVV are selected as the prediction vectors. The next step is to define a cost function which is composed of the error between the RVV and the available prediction vectors. Then, the selected two virtual vectors are evaluated and the one that minimizes the cost function will be applied in the next instant. In this way, only two prediction vectors need to be evaluated and the computation burden is highly alleviated. In the meantime, the weighting factor involved in predictive torque control is avoided. In addition, to achieve the readily implementation with standard pulsewidth modulation switching sequence, 18 virtual vectors are artfully replaced by their corresponding equivalent virtual vectors. Finally, the proposed method is comparatively studied and compared with other benchmark methods. Simulation and experimental results are offered to confirm the effectiveness of the proposed method.**

***Index Terms*—Current harmonics, deadbeat current control (DBCC), model predictive control (MPC), multiphase machine, permanent magnet synchronous machine (PMSM) motor, reference voltage vector (RVV), six-phase machine.**

I. Introduction

VARIABLE speed drives of a permanent magnet synchronous machine (PMSM) have been widely used in industrial applications. In particular, multiphase machines are receiving more and more attention due to their high torque density, fault-tolerant capability, and lower power rating per phase [1], [2]. In addition, the model predictive control (MPC) has been recently introduced to the application for high-

Manuscript received May 21, 2018; revised August 7, 2018; accepted September 30, 2018. Date of publication October 8, 2018; date of current version May 2, 2019. This work was supported in part by the Natural Science Foundation of China, China, under Grant 51677159 and in part by the Research Grants Council of HKSAR, China, under Grant CityU 21201216. Recommended for publication by Associate Editor A. J. M. Cardoso. *(Corresponding author: Chunhua Liu.)*

The authors are with the School of Energy and Environment, City University of Hong Kong, Kowloon Tong, Hong Kong and also with Shenzhen Research Institute, City University of Hong Kong, Shenzhen 518057, China (e-mail:

search tree method [21], the sphere decoding algorithm [22], [23], or excluding the inapplicable voltage vectors in advance [24]. Unfortunately, the methods proposed in [21] and [22] are difficult to be implemented. Meanwhile, the lookup table developed in [24] is complicated with two flux position observers involved.

In the aforementioned MPC method for the six-phase machine, either large computation time is required [18]–[20], or complicated predictive model is involved [24]. In addition, Pandit *et al.* [25] fail to implement the virtual vectors using standard pulsewidth modulation (PWM) switching sequence. The MPC method combined with deadbeat current control (DBCC) [15] or DB-DTFC [14] is limited to a three-phase machine and only considers the energy conversion-related subspace, which is not applicable for the two-degree freedom six-phase machine. This paper proposes RVV-based MPC to reduce the computation time and harmonic currents by using a very simple and effective predictive model. The RVV is obtained based on the principle of DBCC. Instead of directly applying the 12 largest actual vectors, 24 virtual vectors are synthesized by the largest actual vectors and the second largest actual vectors to suppress the current harmonics. Then, with the position of the RVV determined, two in-phase virtual vectors closest to the RVV are selected as the prediction vectors. In this way, the number of voltage vector candidates is reduced from 12 to 2. Subsequently, a novel cost function composed of the error between these two virtual vectors and the RVV is defined, where the weighting factor involved in MPTC is absent and the predictive model is simplified. Finally, the conventional MPCC method, the direct DBCC method, and the proposed method are all implemented and compared. Also, experimental results are given to verify the validity of the proposed method.

II. Conventional MPCC Control Scheme

In MPC, the first step is to predict the machine behavior at each sampling period using the discretized model of the machine. Then, a cost function is defined based on the predicted machine state according to the control criteria. For instance, the error between the reference and the predicted stator currents in the α–β plane can be included in the cost function, which is expressed as $g = |i_\alpha^*{-}i_\alpha| + |i_\beta^*{-}i_\beta|$. Subsequently, each available voltage-source inverter (VSI) state is evaluated through solving an optimization problem to minimize the predefined cost function. The optimal voltage vector will be applied in the next instant.

A. Predictive Model

The asymmetrical six-phase PMSM motor studied in this paper has two sets of three-phase windings spatially shifted by 30 electrical degrees with two isolated neutral points. The six-phase PMSM motor is supplied by a six-phase two-level VSI, as shown in Fig. 1. The widely used vector space decomposition (VSD) [26] is adopted to model the asymmetrical six-phase PMSM machine in a decoupled manner. Based on the amplitude invariant

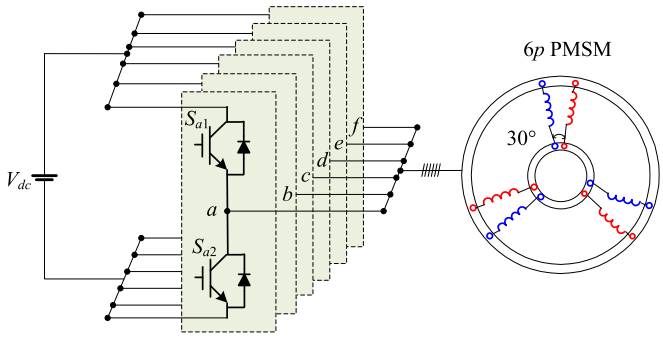

Fig. 1. Scheme of the six-phase PMSM drive.

constraint, the VSD transformation matrix is expressed as

$$T_{\alpha\beta} = \frac{1}{3}\begin{bmatrix} 1 & -\frac{1}{2} & -\frac{1}{2} & \frac{\sqrt{3}}{2} & -\frac{\sqrt{3}}{2} & 0 \\ 0 & \frac{\sqrt{3}}{2} & -\frac{\sqrt{3}}{2} & \frac{1}{2} & \frac{1}{2} & -1 \\ 1 & -\frac{1}{2} & -\frac{1}{2} & -\frac{\sqrt{3}}{2} & \frac{\sqrt{3}}{2} & 0 \\ 0 & -\frac{\sqrt{3}}{2} & \frac{\sqrt{3}}{2} & \frac{1}{2} & \frac{1}{2} & -1 \\ 1 & 1 & 1 & 0 & 0 & 0 \\ 0 & 0 & 0 & 1 & 1 & 1 \end{bmatrix} \tag{1}$$

$$\begin{bmatrix} v_\alpha & v_\beta & v_x & v_y & v_{o1} & v_{o2} \end{bmatrix}^T = T_{\alpha\beta}\begin{bmatrix} v_a & v_b & v_c & v_d & v_e & v_f \end{bmatrix}^T. \tag{2}$$

Using the first two rows in (1), the fundamental components and the harmonics in the order of $12n{\pm}1\,(n = 1, 2, 3\cdots)$ are mapped into the α–β subspace, which governs the energy conversion. The middle two rows in (1) map the harmonics of the order $6n \pm 1$ ($n = 1, 3, 5\cdots$) into the x–y subspace, which does not produce torque but causes additional losses. The last two rows in (1) represent the zero sequence harmonic components in the order of $3n$ ($n = 1, 3, 5\cdots$), which are ignored due to the isolated neutral-point connection.

To obtain the synchronous frame model, the Park transformation is applied to the machine variables in the α–β plane

$$T_{dq} = \begin{bmatrix} \cos\theta & \sin\theta \\ -\sin\theta & \cos\theta \end{bmatrix} \tag{3}$$

$$\begin{bmatrix} v_d & v_q \end{bmatrix}^T = T_{dq}\begin{bmatrix} v_\alpha & v_\beta \end{bmatrix}^T. \tag{4}$$

By using this approach, the practical model of the machine in the synchronous reference frame and the x–y subspace can be obtained as

$$\begin{bmatrix} v_d \\ v_q \end{bmatrix} = \begin{bmatrix} R & -\omega_r L_q \\ \omega_r L_d & R \end{bmatrix}\begin{bmatrix} i_d \\ i_q \end{bmatrix} + \begin{bmatrix} L_d \\ L_q \end{bmatrix} * p * \begin{bmatrix} i_d \\ i_q \end{bmatrix} + \begin{bmatrix} 0 \\ \omega_r \psi_f \end{bmatrix} \tag{5}$$

$$\begin{bmatrix} v_x \\ v_y \end{bmatrix} = \begin{bmatrix} R & 0 \\ 0 & R \end{bmatrix}\begin{bmatrix} i_x \\ i_y \end{bmatrix} + L_l * p * \begin{bmatrix} i_x \\ i_y \end{bmatrix} \tag{6}$$

where v_d and v_q are the stator voltage components in the *d*- and *q*-axis; i_d and i_q are the stator current components in the *d*- and *q*-axis; *R* is the stator resistance; L_d and L_q are the stator inductance in the *d*- and *q*-axis; ω_r is the rotor angular speed; *p* is the time derivative operator; ψ_f is the permanent magnet flux linkage; v_x and v_y are the stator voltage components in the *x*–*y* subspace; i_x and i_y are the stator current components in the *x*–*y* subspace; and L_l is the leakage self-inductance.

The forward Euler method is used to derive the discretized model based on (5) and (6), thus obtaining the predictive model of the machine. The details of how the stator currents at instant $k+1$ are predicted can be found in [16]. Since the energy conversion is only involved in the α–β subspace, the cost function can be defined as

$$g = |i_\alpha^* - i_\alpha(k+1)| + \left|i_\beta^* - i_\beta(k+1)\right|. \tag{7}$$

Or, it is an alternative to take into account the *x*–*y* stator current components in the cost function to suppress current harmonics, which is expressed as

$$\begin{aligned} g = {} & |i_\alpha^* - i_\alpha(k+1)| + \left|i_\beta^* - i_\beta(k+1)\right| \\ & + |i_x^* - i_x(k+1)| + \left|i_y^* - i_y(k+1)\right|. \end{aligned} \tag{8}$$

The current components in the *x*–*y* subspace at instant $k+1$, $i_x(k+1)$, and $i_y(k+1)$ can be predicted in the similar way, using the forward Euler method based on (6). Subsequently, the available voltage vectors can be evaluated by (7) or (8).

B. Prediction Voltage Vectors

The six-phase two-level VSI is characterized with $2^6 = 64$ switching states $[S_a S_b S_c S_d S_e S_f]$. The stator phase voltage can be expressed in the form of the switching states and the dc voltage as follows:

$$\begin{bmatrix} v_a \\ v_b \\ v_c \\ v_d \\ v_e \\ v_f \end{bmatrix} = \frac{V_{\mathrm{dc}}}{3} \begin{bmatrix} 2 & -1 & -1 & 0 & 0 & 0 \\ -1 & 2 & -1 & 0 & 0 & 0 \\ -1 & -1 & 2 & 0 & 0 & 0 \\ 0 & 0 & 0 & 2 & -1 & -1 \\ 0 & 0 & 0 & -1 & 2 & -1 \\ 0 & 0 & 0 & -1 & -1 & 2 \end{bmatrix} \begin{bmatrix} S_a \\ S_b \\ S_c \\ S_d \\ S_e \\ S_f \end{bmatrix} \tag{9}$$

where $S_i = 1\,(i = a,\ b,\ c,\ d,\ e,\ f)$ when the upper switching is ON; and $S_i = 0\,(i = a,\ b,\ c,\ d,\ e,\ f)$ when the upper switching is OFF.

Then, the phase voltages are transformed into the stationary frame using VSD transformation matrix $T_{\alpha\beta}$

$$\boldsymbol{v_{\alpha\beta xyo1o2}} = {T_{\alpha\beta}}^* \boldsymbol{v_{abcdef}}. \tag{10}$$

In this way, the voltage vectors are mapped into two orthogonal subspaces, namely the α–β and *x*–*y* subspaces, as shown in Fig. 2. Each voltage vector in Fig. 2 is identified using the decimal number equivalent to the binary number of $[S_a S_b S_c]$–$[S_d S_e S_f]$. It can be seen from Fig. 2 that there are totally 48 active voltage vectors.

Evaluating all the 48 voltage vectors will be redundant since the computing time is a crucial factor for MPC implementation. A common practice is only evaluating the largest 12 voltage vectors [16]–[19]. Then, the voltage vector that minimizes the cost function will be applied in the next instant.

The above content in this section describes the basic principle of the conventional MPCC method for a six-phase PMSM motor. This method can present fast dynamic response and it is easy to be implemented practically. Unfortunately, evaluating 13 voltage vectors will still cost a large amount of time, compared with the three-phase machine drives, where only seven vectors need to be evaluated. In addition, using cost function (8) can suppress the current harmonics to some extent but the inclusion of the *x*–*y* components will complicate the predictive model while adopting (7) in the conventional MPCC will result in large current harmonics. Besides, the potential of the other active vectors is not fully exploited for the sake of harmonics reduction.

III. Principle of Proposed Method

To overcome the aforementioned problems introduced in the conventional MPCC method, a DBCC-based MPC method using virtual vectors is proposed here. The control diagram of the proposed MPC method is illustrated in Fig. 3, which mainly includes four parts: the RVV calculation based on DBCC, the new cost function design, the prediction vectors synthesization, and the switching pulse generation of the prediction vectors. The details of the proposed method are elaborated in the following text.

A. RVV Calculation

The solution of DBCC is adopted to calculate the desired RVV. The obtained RVV will be included as a reference vector in the cost function to evaluate the feasible prediction vectors. Using the Euler method, namely $di/dt = (i(k+1)\text{–}i(k))/T_s$, (5) can be expressed as

$$\begin{cases} v_d(k) = R_s i_d(k) + \frac{L_d}{T_s}(i_d(k+1) - i_d(k)) + e_d \\ v_q(k) = R_s i_q(k) + \frac{L_q}{T_s}(i_q(k+1) - i_q(k)) + e_q. \end{cases} \tag{11}$$

Then, the phase currents in the *d*- and *q*-axis at instant $k+1$ can be predicted as

$$\begin{cases} i_d(k+1) = \left(1 - \frac{R_s T_s}{L_d}\right) i_d(k) + \frac{L_q}{L_d}\omega_r T_s i_q(k) + \frac{T_s}{L_d} v_d(k) \\ i_q(k+1) = \left(1 - \frac{R_s T_s}{L_q}\right) i_q(k) - \frac{L_d}{L_q}\omega_r T_s i_d(k) + \frac{T_s}{L_q} v_q(k). \end{cases} \tag{12}$$

In digital implementation, the computation delay will be involved caused by the large computation time, which can deteriorate the control performance [14]. A valid solution is using a two-step prediction to compensate the computation delay [14], where the current at instant $k+2$ is predicted as

$$\begin{cases} i_d(k+2) = \left(1 - \frac{R_s T_s}{L_d}\right) i_d(k+1) + \frac{L_q}{L_d}\omega_r T_s i_q(k+1) \\ \qquad\qquad + \frac{T_s}{L_d} v_d(k+1) \\ i_q(k+2) = \left(1 - \frac{R_s T_s}{L_q}\right) i_q(k+1) - \frac{L_d}{L_q}\omega_r T_s i_d(k+1) \\ \qquad\qquad + \frac{T_s}{L_q} v_q(k+1). \end{cases} \tag{13}$$

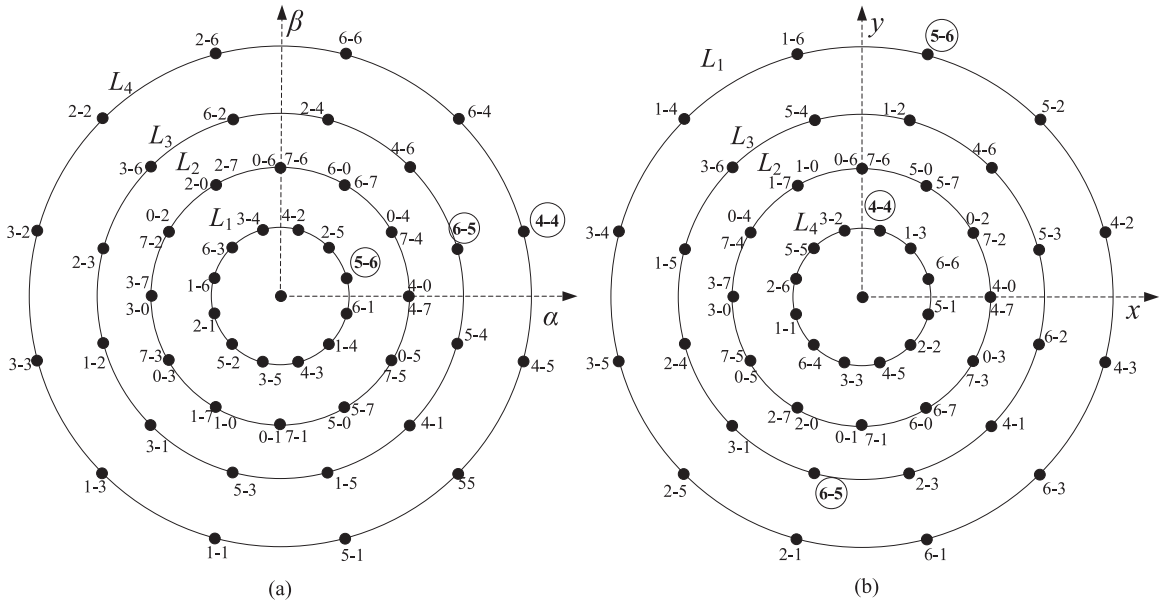

Fig. 2. Actual voltage vectors in the α–β and x–y subspace.

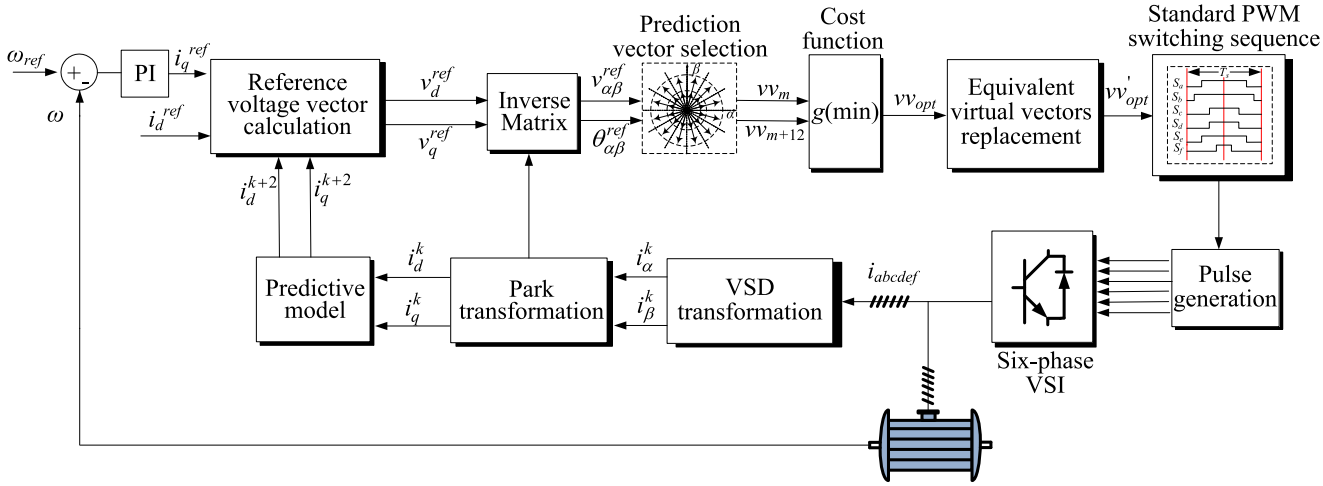

Fig. 3. Control diagram of the proposed MPC method.

According to the DBCC principle, the following constraints should be satisfied:

$$\begin{cases} i_d(k+2) = i_d^{\text{ref}} \\ i_q(k+2) = i_q^{\text{ref}}. \end{cases} \tag{14}$$

Substituting (14) into (13), the d- and q-axis components of the RVV can be expressed as

$$\begin{cases} v_d^{\text{ref}} = R_s i_d(k+1) + \frac{L_d}{T_s}(i_d^{\text{ref}} - i_d(k+1)) + e_d \\ v_q^{\text{ref}} = R_s i_q(k+1) + \frac{L_q}{T_s}(i_q^{\text{ref}} - i_q(k+1)) + e_q. \end{cases} \tag{15}$$

In this way, the expected RVV is obtained, which can be expressed in the form of a complex as

$$v^{\text{ref}} = v_d^{\text{ref}} + j v_q^{\text{ref}} \tag{16}$$

where j is the imaginary unit.

By transforming the RVV in (16) into the α–β plane using the inverse Park transformation, which is given by

$$\begin{pmatrix} v_\alpha^{\text{ref}} \\ v_\beta^{\text{ref}} \end{pmatrix} = \begin{pmatrix} \cos\theta & -\sin\theta \\ \sin\theta & \cos\theta \end{pmatrix} \begin{pmatrix} v_d^{\text{ref}} \\ v_q^{\text{ref}} \end{pmatrix} \tag{17}$$

$$v^{\text{ref}} = v_\alpha^{\text{ref}} + j v_\beta^{\text{ref}}. \tag{18}$$

Subsequently, the position of the RVV in the α–β plane can be obtained by

$$\theta_{\text{ref}} = \arctan\left(\frac{v_\beta^{\text{ref}}}{v_\alpha^{\text{ref}}}\right). \tag{19}$$

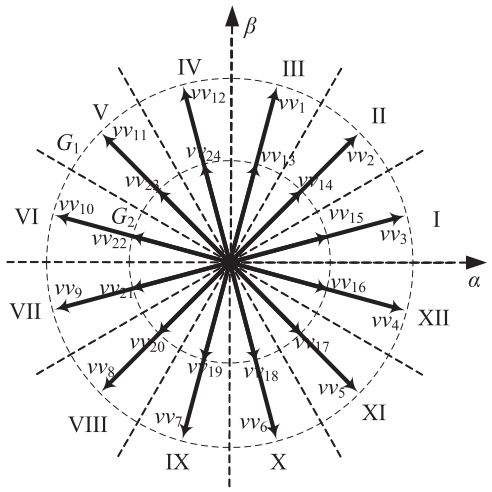

Fig. 4. Diagram of the synthesized virtual vectors and the divided sectors.

B. Prediction Vectors Selection

With the position of the RVV determined, the feasible voltage vectors can be evaluated to select the optimal ones closest to the RVV. The prediction vectors can be the largest 12 vectors from Group L_4 in Fig. 2, as commonly adopted in [16]–[19]. However, the current harmonics fail to be regulated using these 12 actual vectors. An effective approach to suppress the current harmonics is using the virtual vectors which are synthesized by two actual vectors [20], [25]. It can be seen from Fig. 2(a) that voltage vector v_{5-6}, v_{6-5}, and v_{4-4} are aligned in phase in the α–β subspace, while in the *x*–*y* subspace, v_{6-5} is in opposite direction with v_{5-6} and v_{4-4}. Therefore, the effect of vector v_{6-5} on the flux component in the *x*–*y* subspace is opposite with v_{5-6} and v_{4-4}. Meanwhile, the flux components in the *x*–*y* subspace can be expressed as

$$\begin{bmatrix} \psi_x \\ \psi_y \end{bmatrix} = \begin{bmatrix} L_l & 0 \\ 0 & L_l \end{bmatrix} \begin{bmatrix} i_x \\ i_y \end{bmatrix}. \tag{20}$$

According to (20), the flux amplitude in the *x*–*y* subspace is proportional to its harmonic current components. Therefore, weakening the flux amplitude in the *x*–*y* subspace can suppress the harmonic currents. Therefore, the vectors from Group L_3 can be adopted to synthesize a virtual vector to suppress the harmonic currents. There are two options to obtain the virtual vectors, using the actual vectors from Groups L_4 and L_3, or L_3 and L_1 as reported in [25], for the sake of torque ripple reduction. The virtual vectors are synthesized based on the constraint that the sum of the two vectors in the *x*–*y* subspace is zero, for instance, v_{4-4} and v_{6-5}, or v_{5-6} and v_{6-5}. Then, the acting time of each actual vector, as well as the amplitude of the virtual vectors can be calculated. The details of the calculation can be found in [20]. There are totally 24 virtual vectors and specifically, 12 of them with larger amplitude are synthesized by the actual vectors from Groups L_4 and L_3, termed as Group G_1 in Fig. 4; another 12 with smaller magnitude are synthesized by the actual vectors from Groups L_3 and L_1, termed as Group G_2. The amplitude of the virtual vectors from Group G_1 is 0.597 V_{dc} and G_2 is 0.345 V_{dc}. For the virtual vectors from Group G_1, the acting time of the actual vectors from Groups L_4 and L_3 is $0.731T_s$ and $0.269T_s$, respectively. While for the virtual vectors from Group G_2, the acting time of the actual vectors from Groups L_1 and L_3 is $0.422T_s$ and $0.578T_s$, respectively.

With the adopted prediction vectors determined, the optimal ones can be selected based on the position of above-calculated RVV. The α–β plane is divided into 12 sectors by the middle lines of two adjacent virtual vectors, as shown in Fig. 4. Then, the optimal prediction vectors should be located in the same sector with the RVV. For instance, if the calculated RVV lies in Sector I, the virtual vectors vv_3 and vv_{15} should be selected. The prediction vectors can be determined in the same manner when the RVV lies in other sectors. It is noted that there are always only two virtual vectors to be selected, vv_m and vv_{m+12} ($m = 1, 2, 3, \ldots, 12$) no matter where the RVV locates.

C. Cost Function Design

In Section III-B, there are two prediction vectors, vv_m and vv_{m+12} closest to the RVV selected. These two vectors are aligned in phase but with different amplitudes. A novel cost function is designed to evaluate the error between the amplitude of the RVV and these two selected virtual vectors, which is expressed as

$$g = \left| \left| v^{\text{ref}} \right| - \left| vv_i \right| \right| \tag{21}$$

where vv_i represents the selected two virtual vector candidates. These two candidates, along with a null vector, are evaluated by (21) and the one that minimizes (21) will be selected and applied at next instant. It can be seen from (21) that the weighting factor involved in the MPTC method is avoided here. Besides, there are only three candidate vectors to be evaluated and therefore the computing time needed is much smaller. In the meantime, the *x*–*y* harmonics are regulated by the virtual vectors.

D. Switching Pulse Generation

With the optimal virtual vector selected in Section III-C, the switching pulses corresponding to the selected virtual vector should be applied. However, the switching pulses for some of the virtual vectors are not standard PWM pulses in one period, which makes the implementation difficult. According to their different switching pulse generation features, the 24 virtual vectors can be divided into four groups, namely S_1 (vv_1, vv_3, vv_5, vv_7, vv_9, vv_{11}), S_2 (vv_2, vv_4, vv_6, vv_8, vv_{10}, vv_{12}), S_3 (vv_{13}, vv_{15}, vv_{17}, vv_{19}, vv_{21}, vv_{23}), and S_4 (vv_{14}, vv_{16}, vv_{18}, vv_{20}, vv_{22}, vv_{24}). The switching pulse generation for virtual vectors vv_1, vv_2, vv_{13}, and vv_{14} is illustrated in Fig. 5 as examples.

It can be seen from Fig. 5(a) that for virtual vector vv_1, the switching sequence is standard in one PWM period, indicating that it is easy to be implemented. While for virtual vector vv_2, the switching sequence is non-standard since it can be seen from Fig. 5(b) that the level of S_b and S_e is opposite at the middle of the PWM period. In addition, non-standard switching sequences can also be observed in Fig. 5(c) and (d) for virtual vectors vv_{13} and vv_{14}. The switching pulses generation for other virtual vectors can be analyzed in the same manner and only vv_1, vv_3, vv_5, vv_7, vv_9, and vv_{11} among all 24 virtual vectors can present

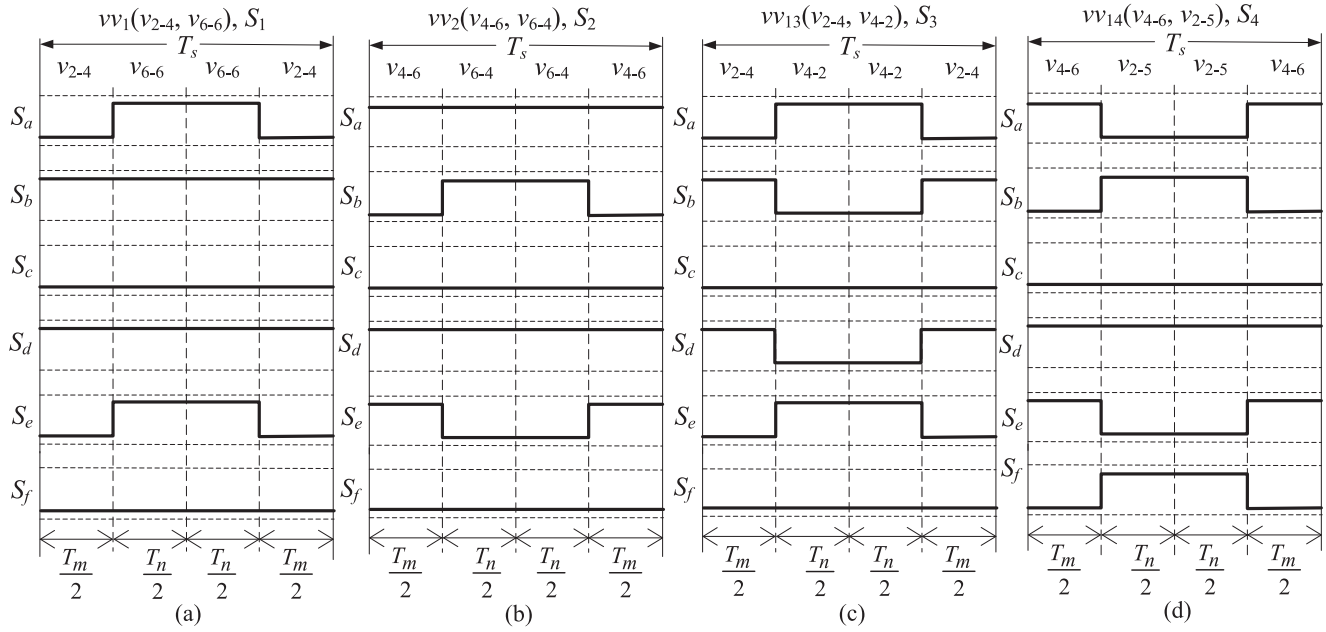

Fig. 5. Switching pulses generation for virtual vectors. (a) vv_1. (b) vv_2. (c) vv_{13}. (d) vv_{14}.

standard PWM switching sequence. Other virtual vectors from S_2, S_3, and S_4 all present non-standard PWM switching sequences.

To achieve easy implementation, a valid solution is adopting the actual vectors from Group L_2 in Fig. 2 to obtain equivalent virtual vectors to replace the virtual vectors with non-standard PWM switching sequence. Due to the different features of the virtual vectors from Groups S_2 and S_3, S_4, the solution of their switching pulses generation will be discussed separately. First, for virtual vectors vv_2, vv_4, vv_6, vv_8, vv_{10}, and vv_{12} from Group S_2, the two vectors from Group L_2 adjacent to the actual vector from Group L_4 in the α–β subspace will be used to form the equivalent vector to replace it. For instance, for virtual vector vv_2, which is synthesized by v_{4-6} and v_{6-4}, the actual vector v_{6-4} can be replaced by two actual vectors v_{0-4} and v_{6-7}, since the sum of v_{0-4} and v_{6-7} is equivalent to v_{6-4} both in α–β and x–y subspaces. Therefore, the virtual vector synthesized by v_{4-6}, v_{0-4}, and v_{6-7} (termed as vv'_2) is equivalent to the virtual vector vv_2. Nevertheless, the virtual vector vv'_2 can present standard PWM switching sequence and is easy to be implemented, as shown in Fig. 6(a). Similarly, other virtual vectors vv_4, vv_6, vv_8, vv_{10}, and vv_{12} can be replaced by virtual vectors vv'_4 (v_{4-0}, v_{5-4}, v_{7-5}), vv'_6 (v_{0-1}, v_{1-5}, v_{5-7}), vv'_8 (v_{1-0}, v_{3-1}, v_{7-3}), $vv'10$ (v_{0-2}, v_{2-3}, v_{3-7}), and vv'_{12} (v_{2-0}, v_{6-2}, v_{7-6}).

For the virtual vectors vv_{13}–vv_{24}, their PWM switching sequence is also non-standard. Unfortunately, the solutions proposed for virtual vectors in S_2 are not applicable here. Even with the actual vectors from Group L_2 employed to obtain equivalent vectors to replace the vectors from Group L_1 or L_3, their PWM switching sequence is still non-standard. It can be seen that there is always one vector from Group G_2 aligning in phase with one virtual vector from Group G_1, and the amplitude of G_2 is 57.8% of G_1. Since the standard switching sequence generation for virtual vectors vv_1–vv_{12} has been solved above, inserting a null vector to adjust the duty ratio of vv_1, vv'_2, vv_3, vv'_4, vv_5, vv'_6, vv_7, vv'_8, vv_9, vv'_{10}, vv_{11}, and vv'_{12} can obtain virtual vectors equivalent to vv_{13}–vv_{24} while presenting standard switching sequence simultaneously. For instance, the virtual vector vv_{13} is replaced by an equivalent virtual vector vv'_{13}, which is synthesized by v_{2-4}, v_{6-6}, v_{0-0}, and v_{7-7}, as shown in Fig. 6(b). Moreover, the virtual vector vv'_{14} synthesized by v_{0-4}, v_{4-6}, v_{6-7}, v_{0-0}, and v_{7-7} is adopted to replace vv_{14}.

The next step is to calculate the duration of the null vectors. The amplitude of the virtual vectors from Groups G_1 and G_2 is: $|vv_{G1}| = 0.597\,\mathrm{V_{dc}}$, $|vv_{G2}| = 0.345\,\mathrm{V_{dc}}$. To obtain the vectors equivalent to the virtual vectors in Group G_2, the duration of the null vectors inserted into vectors in G_1 can be calculated as

$$T_z = T_s - \frac{0.345V_{\mathrm{dc}}}{0.597V_{\mathrm{dc}}}T_s = 0.422T_s. \tag{22}$$

In the meantime, as mentioned above, to achieve harmonic currents suppression, the acting time ratio of the actual vector from Groups L_4 and L_3 is

$$\frac{0.731T_s}{0.269T_s} = 2.717. \tag{23}$$

For the virtual vectors vv'_{13}–vv'_{24}, the acting time of the actual vectors from Group L_4 (or L_2) is T'_m and that of the actual vectors from Group L_3 is T'_n. The following constraints should be satisfied:

$$\begin{cases} \frac{T'_m}{T'_n} = 2.717 \\ T'_m + T'_n = 0.578T_s. \end{cases} \tag{24}$$

Solving (24), T'_m and T'_n can be obtained as $T'_m = 0.422T_s$ and $T'_n = 0.156T_s$.

According to the aforementioned analysis, the 18 virtual vectors from S_2, S_3, and S_4 with non-standard switching sequence are replaced by another 18 equivalent virtual vectors

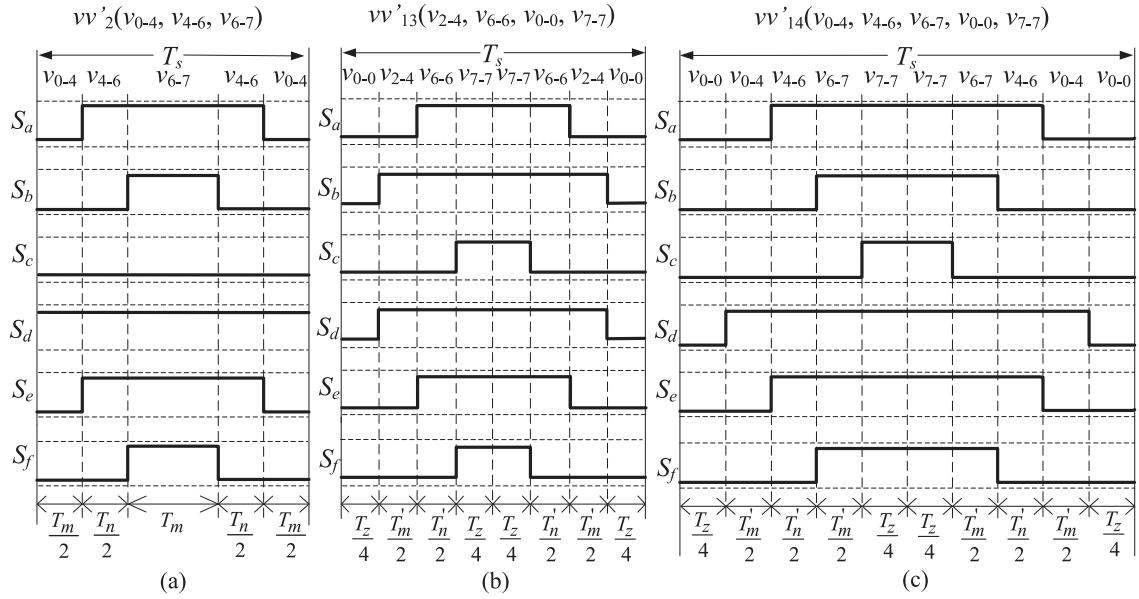

Fig. 6. Switching pulse generation for virtual vectors. (a) vv'_2. (b) vv'_{13}. (c) vv'_{14}.

with standard PWM switching sequence. Now, all 24 virtual vectors can be easily implemented.

Generally, the core idea of the proposed method is consistent with the conventional MPCC method, namely looking for the optimal voltage vector through a cost function. However, they are realized in different manners. The calculation of the RVV is not involved in the conventional MPCC method, where the optimal voltage vector is obtained indirectly based on the cost function with the constraint of current errors, while the proposed MPCC calculates the RVV first and then defines a cost function to compare the RVV with the candidate voltage vectors directly. Compared with the conventional MPCC method, the number of prediction vectors is significantly reduced and the predictive model is simplified in the proposed method. In the meantime, the harmonic currents are effectively suppressed using the virtual vectors.

TABLE I
KEY PARAMETERS OF THE MACHINE AND CONTROL SYSTEM

Specification	Value	
	Simulation	Experimentation
Rated motor power	11 kW	1.1 kW
Rated speed	1500 rpm	1500 rpm
Rated torque	70 Nm	7 Nm
Number of pole pairs	3	3
Stator resistance	4.5 Ω	4.5 Ω
d-axis inductance	0.035 H	0.035 H
q-axis inductance	0.055 H	0.055 H
Permanent magnet flux	0.55 Wb	0.225 Wb
Rotary inertia	0.021 kg*m^2	0.0011 kg*m^2
Rotary inertia of the load machine	---	0.0037 kg*m^2

IV. SIMULATION PERFORMANCES

In this section, the simulations are carried out in the environment of MATLAB/Simulink to verify the effectiveness of the proposed method. The conventional MPCC method and the direct DBCC method are both implemented as benchmark methods. The former one is characterized as directly evaluating the largest 12 voltage vectors using the cost function (8), and the latter one is defined as using two active adjacent vectors and one zero vector from Group L_4 to synthesize the obtained vector in (18). An 11-kW asymmetrical six-phase motor is used in the simulation. The parameters of the machine are listed in Table I. The sampling frequency is set as 10 kHz for all methods in the simulation.

First, the steady-state performance is investigated when the machine is running at 800 r/min with 70-N·m load. It can be seen from Fig. 7 that the amplitude of the phase current reaches 15 A at 70 N·m. The current quality of the direct DBCC and conventional MPCC method is much poorer than the proposed method due to the large amount of harmonic currents in the *x–y* subspace while it is observed that the harmonic currents of the proposed method are almost zero and sinusoidal phase currents are presented. In the meantime, it can be seen that the magnitude of the harmonic currents of the direct DBCC is larger than the conventional MPCC. This can be explained by the fact that the *x–y* components are included in the conventional MPCC and they are slightly suppressed at some extent while the direct DBCC method fails to regulate the *x–y* subspace harmonics.

Second, the dynamic response with a sudden load change of the machine is investigated, as shown in Fig. 8. The load is changed from 35 to 70 N·m at 0.5 s. It can be seen that the torque command is tracked smooth and fast. The phase current quality is also consistent with the performance in Fig. 7. In addition, the current quality is better at 70 N·m than 35 N·m for the direct DBCC and conventional MPCC method.

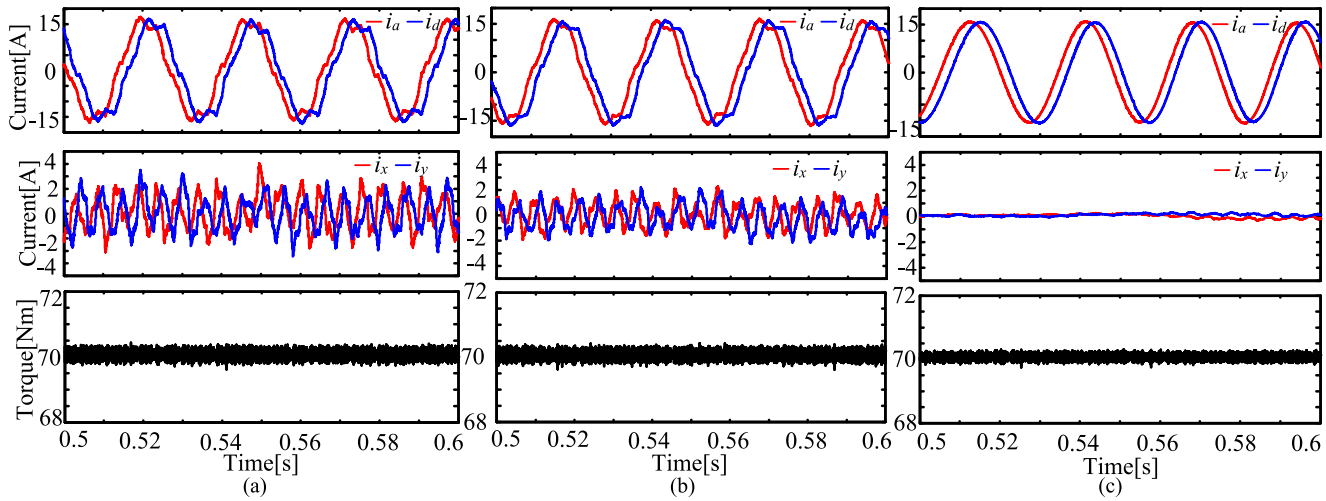

Fig. 7. Steady-state performance of the machine under 800 r/min with 70-N·m load. (a) Direct DBCC method. (b) Conventional MPCC method. (c) Proposed method.

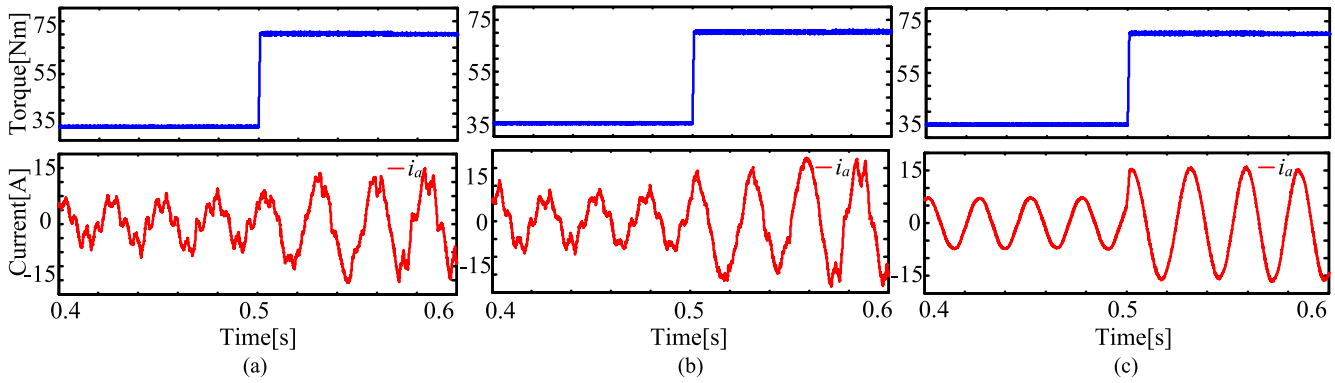

Fig. 8. Dynamic response with sudden load change under 800 r/min. (a) Direct DBCC method. (b) Conventional MPCC method. (c) Proposed method.

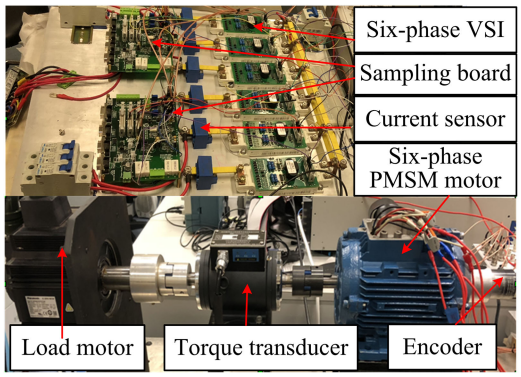

Fig. 9. Experimental setup.

V. Experimental Performances

In this section, the experiments have been conducted to demonstrate the effectiveness of the proposed method. The experimental platform is shown in Fig. 9. The scaled-down 1.1-kW asymmetrical six-phase PMSM motor is supplied by a conventional six-phase two-level VSI with a single dc power supply. The control actions are performed using the DSP (TMS320F28335) from Texas Instruments. The parameters of the PMSM motor drives and its rated values are listed in Table I. It is worth to mention that to better show the superiority of the proposed method, the method presented in [20] is also conducted through experimentation, where the virtual vectors from Group G_1 are evaluated through the cost function (7).

The switching frequency of the direct DBCC method is constant inherently. However, in the MPC methods including the conventional MPCC and the proposed method, the switching frequency is variable. In the meantime, the average switching frequency of the proposed MPC is somewhat higher than the conventional MPCC under the same sampling frequency. This is because there are always two active vectors to be applied in each sampling period of the proposed MPC and the switching state changes twice in some periods. Therefore, the proposed MPC is implemented under 10 and 5 kHz, while the conventional MPCC is implemented 10 kHz to ensure that the switching frequency of the conventional MPCC is in between the switching frequency of the proposed MPC tests. The method presented in [20] and the method in [24] are also implemented under 10-kHz sampling frequency.

A. Steady-State Performance

First, the steady-state performances of the direct DBCC, conventional MPCC, the method in [20], and the proposed MPC method are investigated. The steady-state responses under 800 r/min with a rated load are shown in Fig. 10. From top to bottom, the waveforms given in Fig. 10 are stator phase currents, harmonic currents in the *x–y* subspace, electromagnetic torque, and motor speed. A significant difference can be observed in terms of the *x–y* harmonic currents between the direct DBCC method, the conventional MPCC, and the proposed MPC method. Large *x–y* harmonic currents are generated in the direct DBCC method and the conventional MPCC method as shown in Fig. 10(a) and (b), while the amount of *x–y* currents is clearly limited due to the use of the virtual vectors as shown in Fig. 10(c). This can be explained by the fact that the *x–y* harmonic currents are ignored in the direct DBCC method, where only the variables in the α–β subspace are regulated. While in the conventional MPCC, though the *x–y* components are included in the cost function, they are not well eliminated since the voltage vector is not zero in the *x–y* subspace. This, in turn, results in a low power quality of the stator currents of the direct DBCC method and the conventional MPCC as shown in Fig. 10(a) and (b). In contrast, the very sinusoidal phase currents are exhibited in the proposed MPC method shown in Fig. 10(d). In the meantime, even with the sampling frequency reduced half, the harmonic currents presented by the proposed MPC method are still much smaller compared with the conventional MPCC method, as shown in Fig. 10(e), though larger sampling step results in this slightly increased current ripple. Then, the steady-state test under 800 r/min without load is investigated as shown in Fig. 11. Similar current performances can be observed that the phase currents are distorted in the direct DBCC method and the conventional MPCC method. In the meantime, it can be seen that the current quality is inferior to that under the full-load condition for each method.

The frequency spectrum of the phase currents is given in Fig. 12. The total harmonic distortion (THD) of phase *a* current for these four methods is obtained as 23.58%, 20.53%, 7.97%, and 13.87%, respectively. The zoom-in plot of the harmonics in the low order is provided for better visualization. The fundamental frequency of the current waveform is 40 Hz (800 r/min) and large amount of fifth and seventh harmonics can be observed in Fig. 12(a) and (b). While in Fig. 12(c) and (d), it can be noticed that the fifth and seventh harmonics as well as the harmonics in the higher order are reduced. In addition, the average switching frequencies of the conventional MPCC, the proposed MPC at 10 and 5 kHz are measured as 3520, 6210, and 3352 Hz, respectively. Thus, it is confirmed that the proposed MPC method can present much better steady-state performance with a lower switching frequency. Though the switching frequency of the direct DBCC method is fixed, its current performance is poor. This is because the direct DBCC and the conventional MPCC always generate voltage in the *x–y* subspace, thus resulting in high harmonic currents. Thanks to the suppression of the *x–y* harmonic components by the synthesized virtual vectors in the proposed MPC method, it is possible to obtain a significant improvement in the phase current power quality with a lower switching frequency. Though the method in [20] can also well suppress the harmonic currents in the *x–y* subspace (THD of $i_a = 8.36\%$), 13 prediction vectors are involved, which will introduce large computation time. Another benefit of the proposed MPC method is its reduced number of iterations since the number of prediction vectors to be evaluated is reduced from 13 to 3. The total execution time of direct DBCC, conventional MPCC, the method in [20], and the proposed method is measured as 31.2, 55.6, 56. 9, and 42.7 μs, respectively. The execution time of the MPC methods is much larger than the direct DBCC method and this is the inherent characteristic of the MPC control that large computation time is usually required. However, compared with the conventional MPCC method, the total execution time of the proposed method is reduced by 23%. The torque performance is also presented in Fig. 10. It can be seen that the torque ripple of the proposed MPC at 10 kHz [see Fig. 10(d)] is slightly smaller than that of the direct DBCC and the conventional MPCC. This can be explained by the fact that there are two groups of vectors with different magnitudes in the proposed method instead of 12 vectors of the same magnitude in the conventional MPCC method.

To further investigate the average switching frequency of the conventional MPCC method and the proposed method, they are measured under different speed conditions with half load and rated load, respectively, as shown in Fig. 13. It can be seen that the proposed method with 10-kHz sampling frequency always introduces the highest average switching frequency in all occasions. While with the sampling frequency lowered to 5 kHz, its average switching frequency is still always slightly lower than that of the conventional MPCC. In the meantime, the phase current THD of the proposed method, the conventional MPCC, the method presented in [24], and the direct DBCC with different load conditions under 500 and 1000 r/min are illustrated in Fig. 14(a) and (b). It can be seen that the proposed method can significantly reduce the current THD compared with the conventional MPCC and direct DBCC under the same sampling frequency. Even with the sampling frequency lowered half, the proposed method still presents less phase current THD than the direct DBCC and conventional MPCC thanks to the regulation of the *x–y* harmonic components by virtual vectors. Though the harmonic currents are already effectively suppressed in [24], it is still slightly larger than the proposed method as shown in Fig. 14. It can be justified that in [24], the voltage components in the *x–y* subspace cannot be suppressed to zero theoretically or practically. In the meantime, the predictive model is significantly simplified using the proposed method. This is because the prediction of the torque and flux in each sampling period using the method in [24] is avoided in the proposed method. Moreover, there is no need to tune the weighting factor.

B. Dynamic Responses With Change in Load

Second, to further evaluate the control performance of the proposed method, the dynamic test with a step load change is carried out. At the start, the motor is running at 800 r/min

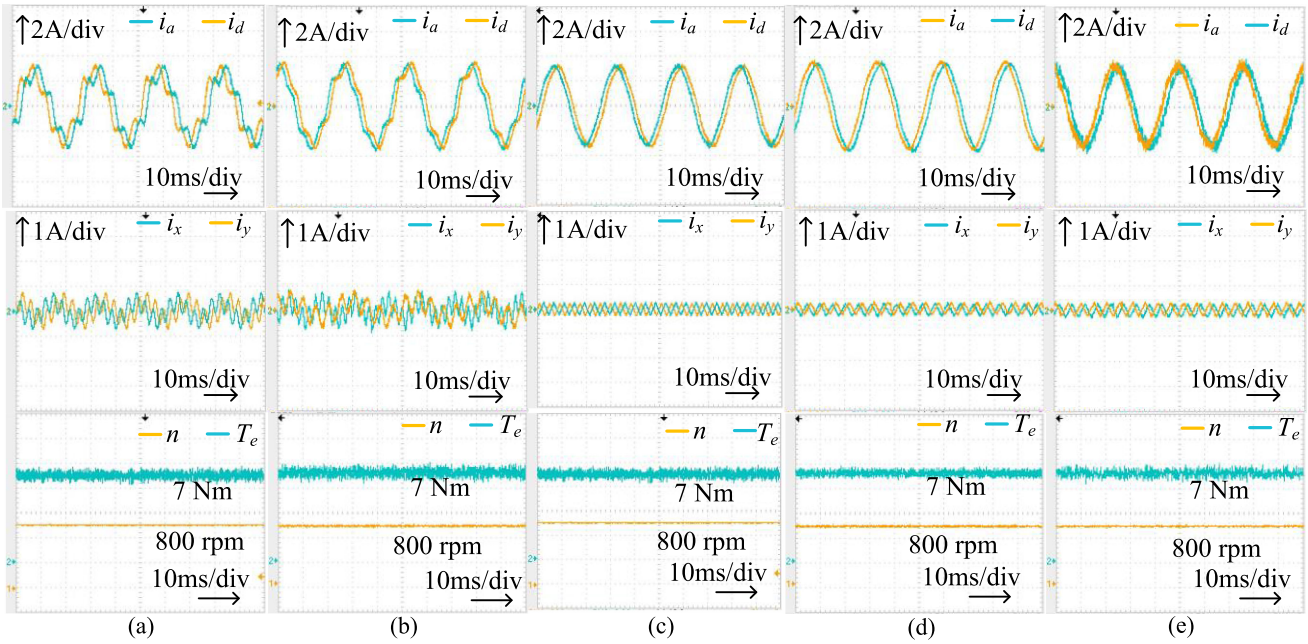

Fig. 10. Test 1 for all these three methods in steady state with full load. From top to bottom: the measured phase currents; the current in the x–y subspace; the electromagnetic torque; and the motor speed. (a) Direct DBCC method. (b) Conventional MPCC method. (c) Method in [20]. (d) Proposed method with 10-kHz sampling frequency. (e) Proposed method with 5-kHz sampling frequency.

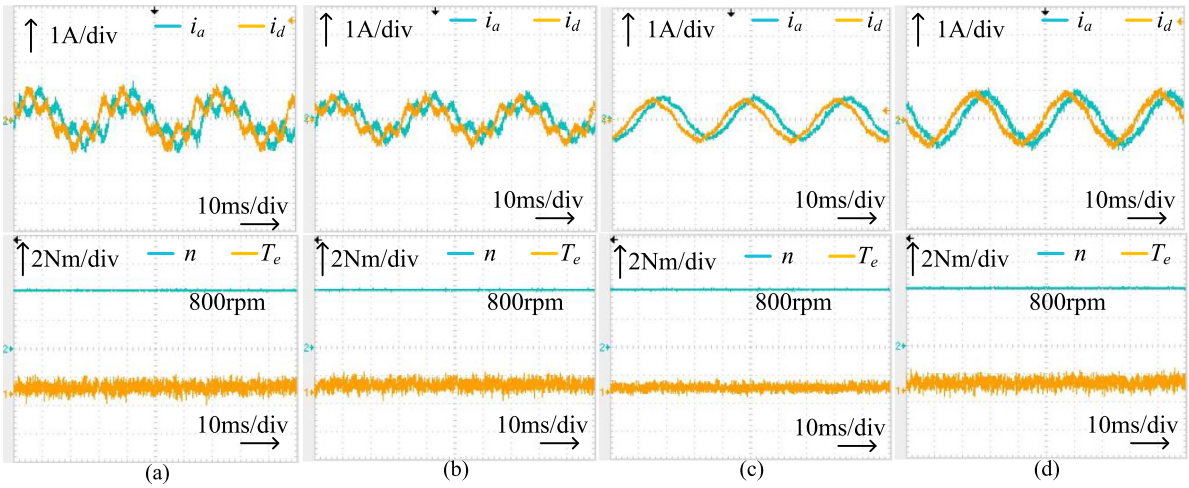

Fig. 11. Test 2 for all these three methods in a steady state without load. From top to bottom: the measured phase currents; the motor speed; and the electromagnetic torque. (a) Direct DBCC method. (b) Conventional MPCC method. (c) Proposed method with 10-kHz sampling frequency. (d) Proposed method with 5-kHz sampling frequency.

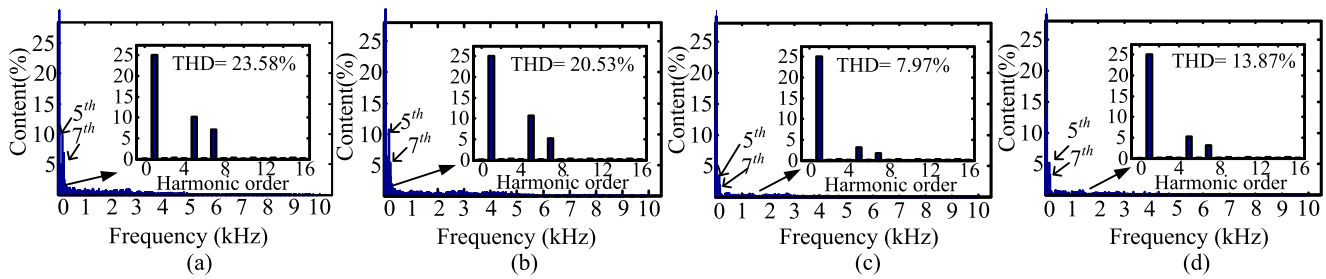

Fig. 12. THD analysis of phase current i_a for all three methods. (a) Direct DBCC method. (b) Conventional MPCC method. (c) Proposed method with 10-kHz sampling frequency. (d) Proposed method with 5-kHz sampling frequency.

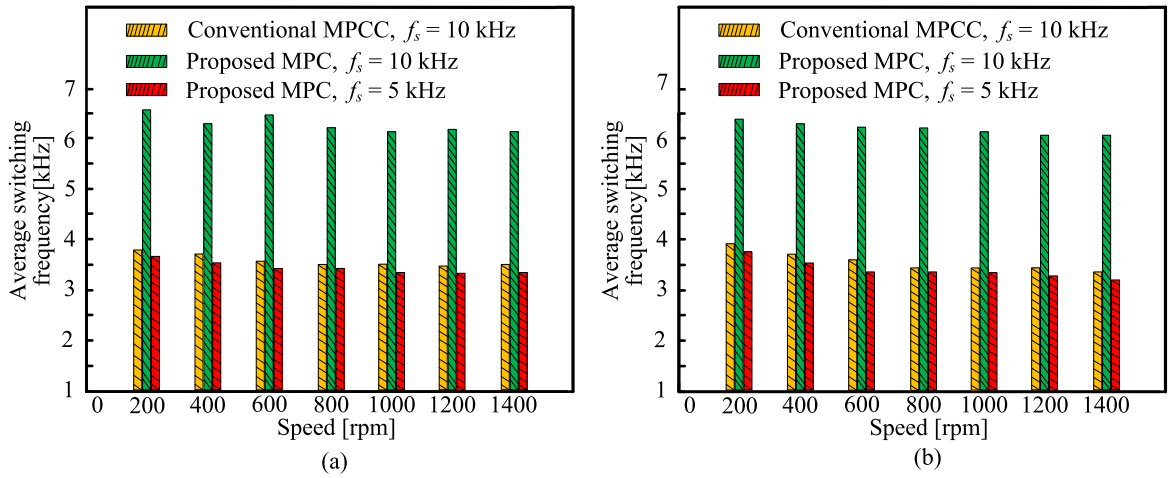

Fig. 13. Measured average switching frequency for all methods under different speed conditions with (a) half load and (b) rated load.

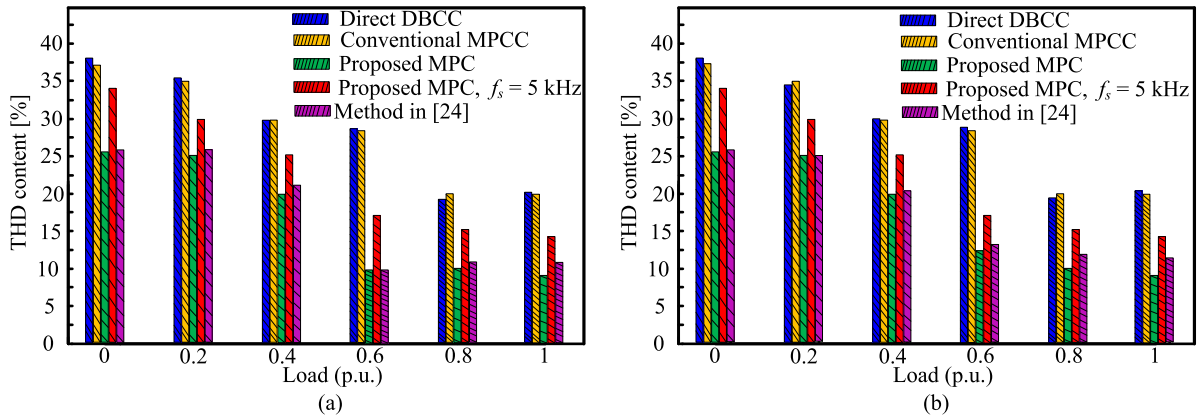

Fig. 14. Phase current THD analysis for all methods under different load conditions under (a) 500 r/min and (b) 1000 r/min.

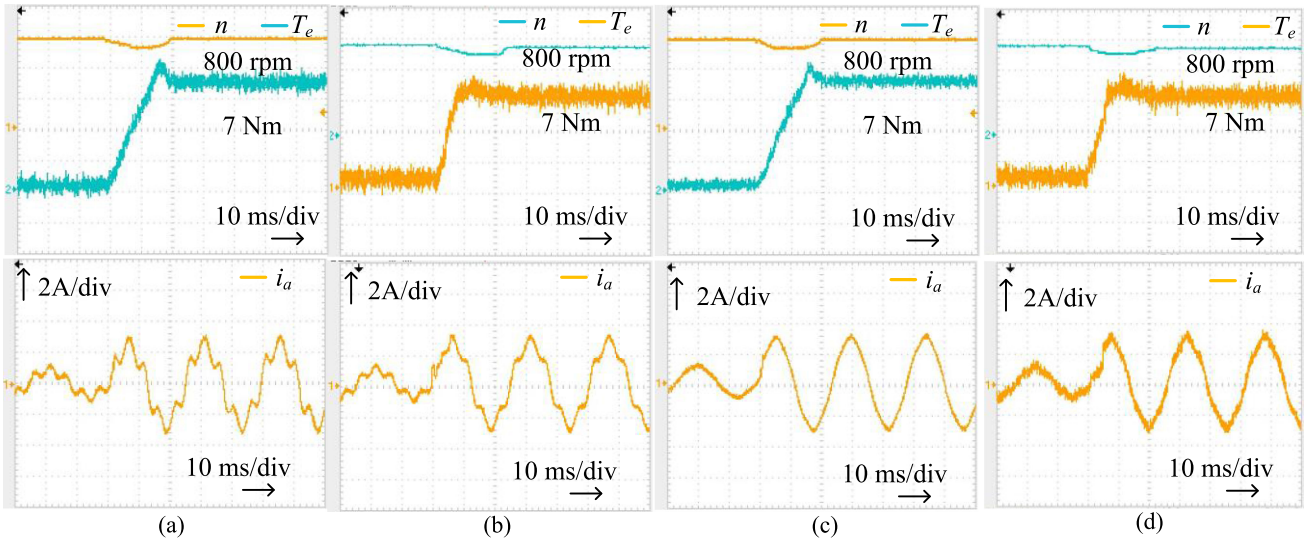

Fig. 15. Test 3 for all methods with sudden load change. From top to bottom: the measure motor speed; the electromagnetic torque; and the phase current. (a) Direct DBCC method. (b) Conventional MPCC method. (c) Proposed method with 10-kHz sampling frequency. (d) Proposed method with 5-kHz sampling frequency.

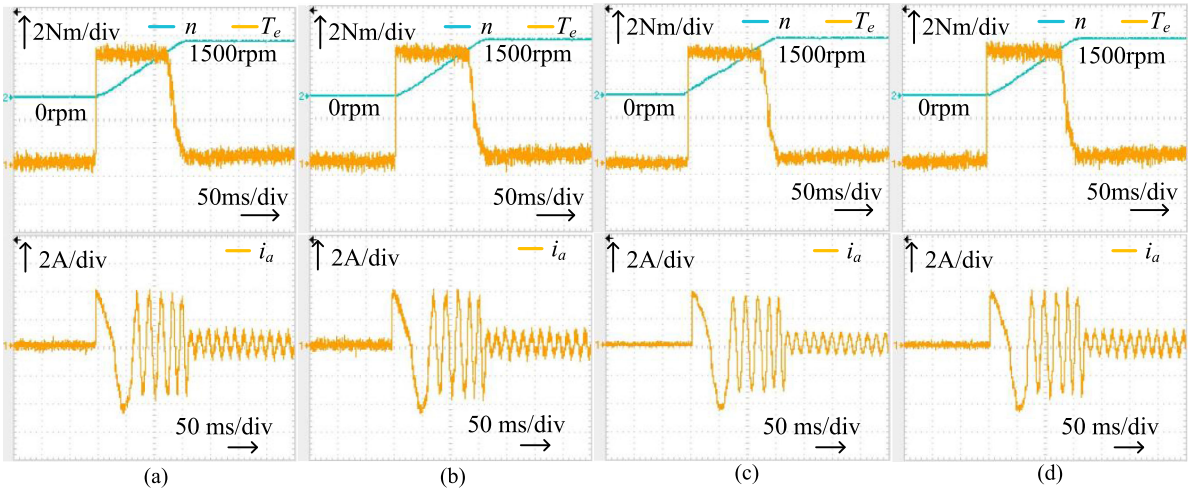

Fig. 16. Test 4 for all methods at acceleration state without load. From top to bottom: the measured rotor speed; the electromagnetic torque; and the phase current. (a) Direct DBCC method. (b) Conventional MPCC method. (c) Proposed method with 10-kHz sampling frequency. (d) Proposed method with 5-kHz sampling frequency.

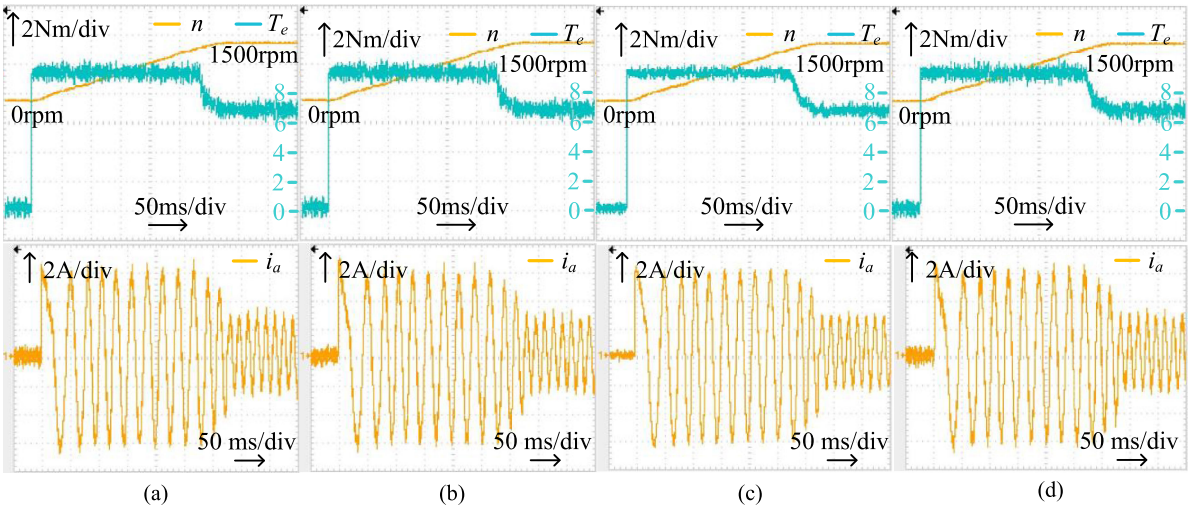

Fig. 17. Test 5 for all methods at acceleration state with full load. From top to bottom: the measured rotor speed; the electromagnetic torque; and the phase current. (a) Direct DBCC method. (b) Conventional MPCC method. (c) Proposed method with 10-kHz sampling frequency. (d) Proposed method with 5-kHz sampling frequency.

and then a rated load is added suddenly. The transient state waveforms are given in Fig. 15, including the speed, electromagnetic torque, and phase current. Fast dynamic response and good disturbance rejection performance can be observed for the conventional MPCC and proposed MPC at 10 and 5 kHz. Additionally, when the motor reaches the steady state, the similar phase current performance with Fig. 10 can be observed.

C. Acceleration Test

Third, the acceleration responses for these three methods are investigated, where the machine accelerates from standstill to 1500 r/min with and without load, respectively. The machine performance under the acceleration without load is illustrated in Fig. 16. It can be observed that the transient state performance of the direct DBCC, conventional MPCC, and the proposed MPC at 10 and 5 kHz is similar. The speed waveforms are smooth without overshoot. However, when the machine speed reaches 1500 r/min, much better current power quality can be observed in Fig. 16(c). This is consistent with the steady-state performance in the first test that the proposed MPC method can present much better power quality phase currents than the direct DBCC and the conventional MPCC method. When a rated load is added to the machine as the acceleration starts, more time is needed to reach the speed command, as shown in Fig. 17. It can be seen that the acceleration time with full load is almost twice of that under the no-load condition. In the meantime, the speed waveforms are still smooth during the transient state.

To sum up, the effectiveness of the x–y harmonic currents regulation of the proposed MPC method in different scenarios is proved by experimental results. In the meantime, the computation burden is reduced, thus making the proposed MPC method more practical. Moreover, the predictive model of the proposed method is more simplified than the conventional MPCC method. Also, the capability of the proposed MPC method to regulate the speed and torque under dynamic conditions is confirmed.

VI. Conclusion

In this paper, a novel RVV-based MPC with harmonic currents suppressed and computation burden reduced is proposed for an asymmetrical six-phase PMSM motor. The major contributions of this work are as follows.

1) Two groups of virtual vectors are synthesized aiming at harmonic currents reduction.
2) The DBCC solution is adopted to calculate the RVV and select the appropriate voltage vector candidates, thus reducing the computing time significantly.
3) A new cost function is defined to directly evaluate the error between the RVV and the selected virtual vectors, which significantly simplifies the predictive model.
4) The 18 virtual vectors with non-standard PWM switching sequences are replaced by the equivalent virtual vectors with the standard PWM switching sequences, where all the virtual vectors can be easily implemented practically.

Accordingly, the simulation and experimental results are both offered to confirm the validity of the proposed MPC method.

References

[1] I. Zoric, M. Jones, and E. Levi, "Arbitrary power sharing among three-phase winding sets of multiphase machines," *IEEE Trans. Ind. Electron.*, vol. 65, no. 2, pp. 1128–1139, Feb. 2018.

[2] E. Levi, "Multiphase electric machines for variable-speed applications," *IEEE Trans. Ind. Electron.*, vol. 55, no. 5, pp. 1893–1909, May 2008.

[3] Y. Zhang, D. Xu, J. Liu, S. Gao, and W. Xu, "Performance improvement of model-predictive current control of permanent magnet synchronous motor drives," *IEEE Trans. Ind. Appl.*, vol. 53, no. 4, pp. 3683–3695, Aug. 2017.

[4] C. Martín, M. R. Arahal, F. Barrero, and M. J. Durán, "Five-phase induction motor rotor current observer for finite control set model predictive control of stator current," *IEEE Trans. Ind. Electron.*, vol. 63, no. 7, pp. 4527–4538, Jul. 2016.

[5] X. Li and P. Shamsi, "Model predictive current control of switched reluctance motors with inductance auto-calibration," *IEEE Trans. Ind. Electron.*, vol. 63, no. 6, pp. 3934–3941, Jun. 2016.

[6] A. Mora, Á. Orellana, J. Juliet, and R. Cárdenas, "Model predictive torque control for torque ripple compensation in variable-speed PMSMs," *IEEE Trans. Ind. Electron.*, vol. 63, no. 7, pp. 4584–4592, Jul. 2016.

[7] F. Wang *et al.*, "Finite control set model predictive torque control of induction machine with a robust adaptive observer," *IEEE Trans. Ind. Electron.*, vol. 64, no. 4, pp. 2631–2641, Apr. 2017.

[8] W. Xie *et al.*, "Finite-control-set model predictive torque control with a deadbeat solution for PMSM drives," *IEEE Trans. Ind. Electron.*, vol. 62, no. 9, pp. 5402–5410, Sep. 2015.

[9] A. A. Ahmed, B. K. Koh, H. S. Park, K. B. Lee, and Y. I. Lee, "Finite-control set model predictive control method for torque control of induction motors using a state tracking cost index," *IEEE Trans. Ind. Electron.*, vol. 64, no. 3, pp. 1916–1928, Mar. 2017.

[10] S. A. Davari, D. A. Khaburi, and R. Kennel, "An improved FCS-MPC algorithm for an induction motor with an imposed optimized weighting factor," *IEEE Trans. Power Electron.*, vol. 27, no. 3, pp. 1540–1551, Mar. 2012.

[11] P. Cortes *et al.*, "Guidelines for weighting factors design in model predictive control of power converters and drives," in *Proc. IEEE Int. Conf. Ind. Technol.*, 2009, pp. 1–7.

[12] Y. Zhang and H. Yang, "Two-vector-based model predictive torque control without weighting factors for induction motor drives," *IEEE Trans. Power Electron.*, vol. 31, no. 2, pp. 1381–1390, Feb. 2016.

[13] C. A. Rojas, J. Rodriguez, F. Villarroel, J. R. Espinoza, C. A. Silva, and M. Trincado, "Predictive torque and flux control without weighting factors," *IEEE Trans. Ind. Electron.*, vol. 60, no. 2, pp. 681–690, Feb. 2013.

[14] X. Zhang and B. Hou, "Double vectors model predictive torque control without weighting factor based on voltage tracking error," *IEEE Trans. Power Electron.*, vol. 33, no. 3, pp. 2368–2380, Mar. 2018.

[15] Y. Zhang, D. Xu, J. Liu, S. Gao, and W. Xu, "Performance improvement of model-predictive current control of permanent magnet synchronous motor drives," *IEEE Trans. Ind. Appl.*, vol. 53, no. 4, pp. 3683–3695, Aug. 2017.

[16] F. Barrero, M. R. Arahal, R. S. Toral, and M. J. Duran, "A proof of concept study of predictive current control for VSI-driven asymmetrical dual three-phase AC machines," *IEEE Trans. Ind. Electron.*, vol. 56, no. 6, pp. 1937–1954, Jun. 2009.

[17] F. Barrero, M. R. Arahal, R. S. Toral, and M. J. Duran, "One-step modulation predictive current control method for the asymmetrical dual three-phase induction machine," *IEEE Trans. Ind. Electron.*, vol. 56, no. 6, pp. 1974–1983, Jun. 2009.

[18] F. Barrero, J. Prieto, E. Levi, and R. Gergor, "An enhanced predictive current control method for asymmetrical six-phase motor drives," *IEEE Trans. Ind. Electron.*, vol. 58, no. 8, pp. 3242–3252, Aug. 2011.

[19] M. J. Duran, J. Prieto, F. Barrero, and S. Toral, "Predictive current control of dual three-phase drives using restrained search techniques," *IEEE Trans. Ind. Electron.*, vol. 58, no. 8, pp. 3253–3263, Aug. 2011.

[20] I. Gonzalez-Prieto, M. J. Duran, J. J. Aciego, C. Martin, and F. Barrero, "Model predictive control of six-phase induction motor drives using virtual voltage vectors," *IEEE Trans. Ind. Electron.*, vol. 65, no. 1, pp. 27–37, Jan. 2017.

[21] A. Linder and R. Kennel, "Model predictive control for electrical drives," in *Proc. IEEE 36th Power Electron. Spec. Conf.*, Jun. 2005, pp. 1793–1799.

[22] T. Geyer and D. E. Quevedo, "Multistep finite control set model predictive control for power electronics," *IEEE Trans. Power Electron.*, vol. 29, no. 12, pp. 6836–6846, Dec. 2014.

[23] T. Geyer and D. E. Quevedo, "Performance of multistep finite control set model predictive control for power electronics," *IEEE Trans. Power Electron.*, vol. 30, no. 3, pp. 1633–1644, Mar. 2015.

[24] Y. Luo and C. Liu, "A simplified model predictive control for a dual three-phase PMSM motor with reduced harmonic currents," *IEEE Trans. Ind. Electron.*, vol. 65, no. 11, pp. 6079–6089, Nov. 2018.

[25] J. K. Pandit, M. V. Aware, R.V. Nemade, and E. Levi, "Direct torque control scheme for a six-phase induction motor with reduced torque ripple," *IEEE Trans. Power Electron.*, vol. 32, no. 9, pp. 7118–7129, Sep. 2017.

[26] Y. Zhao and T. Lipo, "Space vector PWM control of dual three-phase induction machine using vector space decomposition," *IEEE Trans. Ind. Appl.*, vol. 31, no. 5, pp. 1100–1109, Sep./Oct. 1995.

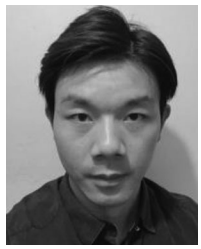

Yixiao Luo (S'16) received the B.Eng. degree from Wuhan University, Wuhan, China, in 2013, and the M.Eng. degree from Hanyang University, Seoul, South Korea, in 2015, both in electrical engineering. He is currently working toward the Ph.D. degree in electrical engineering at the City University of Hong Kong, Kowloon Tong, Hong Kong.

His research interests include power electronics and multiphase machine drives.

Chunhua Liu (M'10–SM'14) received the B.Eng. and M.Eng. degrees in automatic control from the Beijing Institute of Technology, Beijing, China, 2002 and 2005, respectively and the Ph.D. degree in electrical and electronic engineering from The University of Hong Kong, Pokfulam, Hong Kong, in 2009.

He currently serves as an Assistant Professor with the School of Energy and Environment, City University of Hong Kong, Kowloon Tong, Hong Kong. His research interests include electrical energy and power technology, including electric machines and drives, electric vehicles, electric robotics and ships, renewables and microgrid, and wireless power transfer. In these areas, he has published more than 160 refereed papers.

Dr. Liu is currently an Associate Editor for IEEE Transaction on Industrial Electronics, an Editor for the IEEE Transactions on Vehicular Technology, and a Guest Editor-in-Chief for the IEEE Transactions on Energy Conversion. He is also an Editor of *Energies*, a Subject Editor of *IET Renewable Power Generation*, an Associate Editor of Cambridge University—*Wireless Power Transfer*, an Associate Editor for IEEE Chinese Journal of Electrical Engineering, an Editor for IEEE Transactions on Magnetics—Conference. In addition, he is Chair and Founder, HK Chapter, IEEE Vehicular Technology Society.